Geant4 simulation of the n_TOF-EAR2 neutron beam: Characteristics and prospects

Article *in* European Physical Journal A · April 2016

DOI: 10.1140/epja/i2016-16100-8

EPJ A
Hadrons and Nuclei

EPJ.org
your physics journal

Eur. Phys. J. A (2016) **52**: 100 DOI 10.1140/epja/i2016-16100-8

Geant4 simulation of the n_TOF-EAR2 neutron beam: Characteristics and prospects

J. Lerendegui-Marco, S. Lo Meo, C. Guerrero, M.A. Cortés-Giraldo, C. Massimi, J.M. Quesada, M. Barbagallo, N. Colonna, D. Mancusi, F. Mingrone, M. Sabaté-Gilarte, G. Vannini, V. Vlachoudis and the n_TOF Collaboration

Società Italiana di Fisica

Springer

Eur. Phys. J. A (2016) **52**: 100
DOI 10.1140/epja/i2016-16100-8

THE EUROPEAN PHYSICAL JOURNAL A

Regular Article – Experimental Physics

Geant4 simulation of the n_TOF-EAR2 neutron beam: Characteristics and prospects

J. Lerendegui-Marco[1,a], S. Lo Meo[2,3], C. Guerrero[1], M.A. Cortés-Giraldo[1], C. Massimi[3,4], J.M. Quesada[1], M. Barbagallo[5], N. Colonna[5], D. Mancusi[6], F. Mingrone[3], M. Sabaté-Gilarte[1,6], G. Vannini[3,4], V. Vlachoudis[6], and the n_TOF Collaboration[7,b]

[1] Dpto. de Física Atómica, Molecular y Nuclear, Universidad de Sevilla, 41012 Sevilla, Spain
[2] ENEA, Research Centre "Ezio Clementel", I-40129 Bologna, Italy
[3] INFN, Section of Bologna, I-40127 Bologna, Italy
[4] Physics and Astronomy Dept. "Alma Mater Studiorum", University of Bologna, I-40126 Bologna, Italy
[5] INFN, Section of Bari, I-70125 Bari, Italy
[6] CEA-Saclay, F-91191 Gif-sur-Yvette CEDEX, France
[7] European Organization for Nuclear Research (CERN), CH-1211 Geneva, Switzerland

Received: 12 January 2016
Published online: 21 April 2016 –
Communicated by C. Broggini

Abstract. The characteristics of the neutron beam at the new n_TOF-EAR2 facility have been simulated with the Geant4 code with the aim of providing useful data for both the analysis and planning of the upcoming measurements. The spatial and energy distributions of the neutrons, the resolution function and the in-beam γ-ray background have been studied in detail and their implications in the forthcoming experiments have been discussed. The results confirm that, with this new short (18.5 m flight path) beam line, reaching an instantaneous neutron flux beyond 10^5 n/μs/pulse in the keV region, n_TOF is one of the few facilities where challenging measurements can be performed, involving in particular short-lived radioisotopes.

1 Introduction and motivation

Neutron-induced reaction cross sections play a key role in many fields ranging from basic nuclear physics to fission [1] and fusion [2] technologies, astrophysics [3], and nuclear medicine [4,5], among others. These cross sections are usually measured at neutron beam facilities, the most versatile of these being neutron time-of-flight facilities making use of pulsed beams covering a wide range of energies (up to 10 orders of magnitude between meV to GeV). Examples of these are n_TOF [6,7] at CERN in Switzerland, GELINA [8] at IRMM in Belgium, ANNRI [9] at J-PARC in Japan and DANCE [10] at LANL in USA. Very recently the n_TOF Collaboration has built a new neutron beam line, so-called n_TOF-EAR2 [7], with a flight path of 18.5 m (sketched in fig. 1), ten times shorter than the 185 m of the existing n_TOF-EAR1 [6]. Given its high instantaneous flux, this new neutron beam line is specially well suited for measurement of samples with high activity or available only in small quantities. The facility is currently in its commissioning phase, *i.e.* a series of experimental campaigns are being carried out in order to determine the flux, spatial and energy distributions of the neutron beam, the associated backgrounds, the resolution broadening, and, in general, its measurement capabilities. However, not all these characteristics can be accurately measured, and certainly not in all the spatial positions and energy ranges of interest. In this context, Monte Carlo simulations become an essential tool for guiding the measurements, helping in their analysis, the interpretation of their results and, more importantly, for planning the upcoming physics experiments.

A first set of simulations was performed and reported in the works by Weiss *et al.* [7] and Barros *et al.* [11] during the design phase of the facility using the FLUKA code. Indeed, FLUKA [12–14] together with PHITS [15] and MCNP [16] are the codes generally used for the simulation of neutron production and transport. However, the fast development of the Geant4 [17] simulation toolkit and the work of Mendoza *et al.* [18] to include evaluated cross section libraries in Geant4 have recently made it possible to rely on this toolkit for the simulation of spallation neutrons. Furthermore, Lo Meo *et al.* [19] have shown in a recent work that a Geant4 simulation of the neutron production in the n_TOF spallation target and their transport

[a] e-mail: jlerendegui@us.es
[b] www.cern.ch/nTOF.

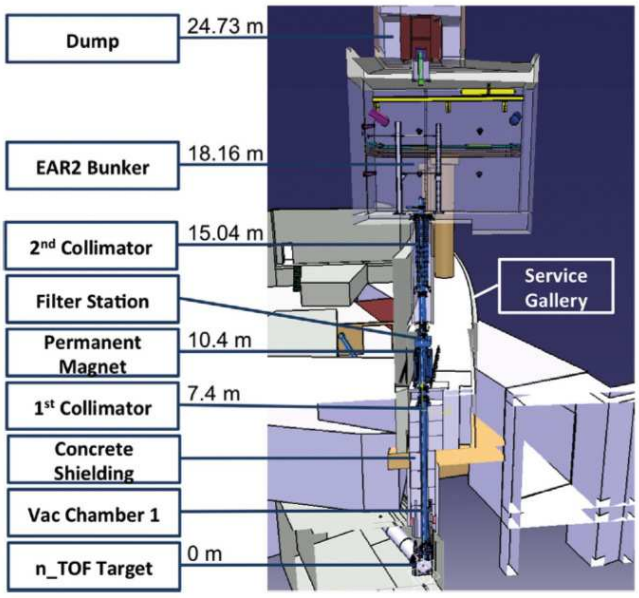

Fig. 1. Layout of the target and EAR2 beam line including the relevant distances from different components to the center of the spallation target.

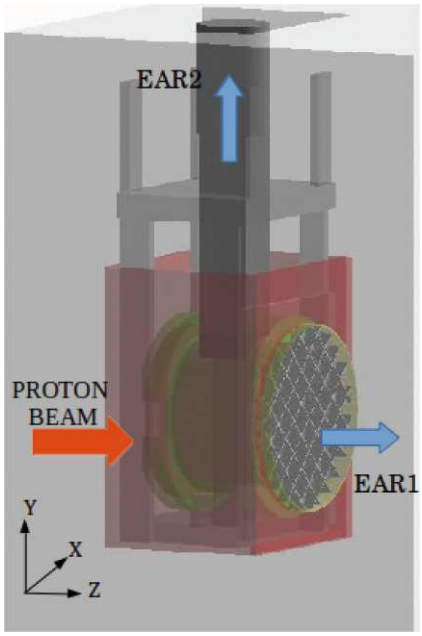

Fig. 2. General view of the spallation target geometry and the beam line towards EAR2 as implemented in Geant4.

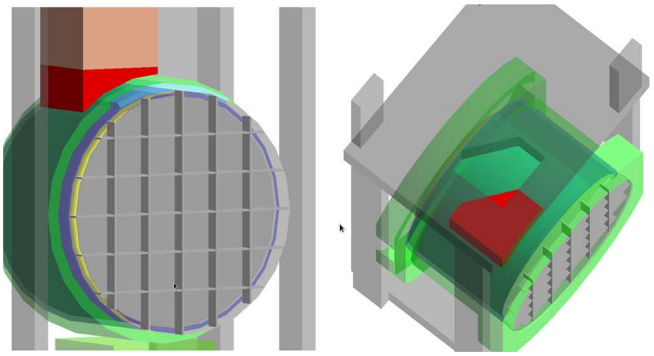

Fig. 3. Detailed view of the target and the vertical exit towards EAR2: Left: front view of the target, semi-dismounted to appreciate the different layers: H_2O cooling and moderator circuits (dark and light blue), Pb core (gray), Al vessel (green) and the beginning of the EAR2 beam line (red). Right: top view showing the upper gap for the beam pipe towards EAR2.

to EAR1 through the beam line is in good agreement with the experimental data, especially regarding the shape of the energy distribution.

In this work we have used this Geant4 application to study the expected characteristics of the neutron beam in n_TOF-EAR2, adressing some aspects not included in previous works, such as the comparison of the neutron flux with those of other time-of-flight facilities, the study of the resolution broadening on actual cross section resonances or the estimation and the effect of the in-beam γ-ray background in neutron capture detectors. This work does not include comparisons with any experimental data because the commissioning measurements are still under analysis, using some of the results presented herein for their interpretation.

In the following section we describe briefly the n_TOF-EAR2 facility and give the details of our simulation code: geometry, physics, scoring and optical transport. The results in terms of average and instantaneous neutron flux, including the comparison with other facilities, are discussed in sect. 3. The spatial profile of the neutron beam at different measuring position is discussed in sect. 4 while sect. 5 deals with the resolution broadening and its effect on cross section resonances. Last, the in-beam γ-ray background and its expected effect on neutron capture measurements are discussed in sect. 6.

2 Geant4 simulation

2.1 Geometry and scoring

The neutrons at the n_TOF facility are generated through spallation of 20 GeV/c protons extracted from the CERN Proton Synchroton, impinging on a thick lead target. These bunches feature a nominal intensity of $7 \cdot 10^{12}$ protons and hit the target with a maximum repetition rate of 0.4 Hz. The spallation neutrons are partially moderated and travel towards the experimental areas along two beam lines: EAR1 at 185 m (horizontal) [6] and EAR2 at 18.5 m (vertical) [7].

The spallation target is shared by the EAR1 and EAR2 beam lines, therefore in this work we have used the detailed geometry already implemented in our previous work about EAR1 [19]. The general view of the target assembly as implemented in Geant4, displayed in fig. 2, shows the target vessel, the surrounding structures, the concrete pit in which it is mounted and the beam line exits towards both experimental areas. Figure 3 shows a more detailed view of the vertical exit towards EAR2 including

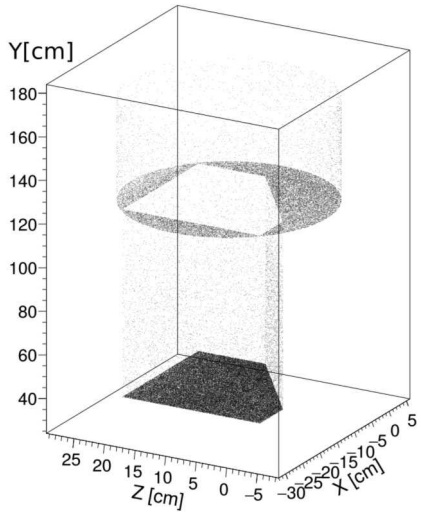

Fig. 4. Projections of the 3D distribution of the scored neutrons, showing that the majority, but not all, of the scored neutrons enter through one of the planes (37 or 123 cm above the lead target axis) orthogonal to the beam direction.

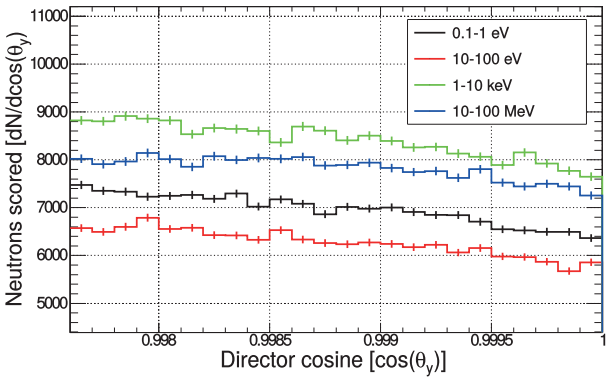

Fig. 5. Direction distribution of neutrons registered in the scoring volume, showing a behavior independent of the neutron energy.

the complex shape of the beam pipe entrance. The neutrons emitted vertically from the lead target are first moderated in a layer of 1.5–3 cm of demineralized water and then traverse the 3 cm thick aluminium vessel that surrounds the target assembly (see fig. 3). The entrance to the beam pipe presents a section that resembles a sort of truncated triangle, hereafter called *irregular*, and is off-centered with respect to the target axis, following accurately the technical drawings.

The Monte Carlo simulation tallies all neutrons and photons entering the vertical beam line, through either its base or its sides, up to 170 cm from the center of the target, with an angle smaller than 4 degrees with respect to the vertical axis, as particles with larger angles do not reach EAR2. The information saved in each scoring is: particle type (neutron or photon), position, direction, energy and time. To visualize the 3-dimensional structure of the scoring volume, we present in fig. 4 the spatial distribution of the scored neutrons. In this figure one can appreciate the details on the geometry, showing the profile of the *irregular* tube attached to target vessel. This 3-dimensional scatter indicates that most of the scored neutrons enter through one of the planes (at 37 or 123 cm) orthogonal to the beam direction, but also that the fraction of neutrons entering through the sides of the beam line is not negligible, demonstrating the importance of considering an extended scorer along the vertical axis.

2.2 Geometrical transport through the beam line

The Geant4 simulation ends when the neutrons or photons enter the scoring volume described above. From there the particles are transported to the experimental area (see fig. 1), but this can not be done via detailed simulations because the angle subtended by the entrance to EAR2 is only 0.032 degrees, and thus only a tiny fraction of the neutrons produced at the target reaches EAR2. For instance, a total of 1000 years of CPU time would be needed to fully simulate the neutron production and transport to EAR2 for a single n_TOF pulse of $7 \cdot 10^{12}$ protons. This CPU time is estimated considering the cluster (Universidad de Sevilla) of 586 computing cores (AMD Abu Dhabi 6344 2.6 GHz/16 MB L3) used for this work.

Therefore, to avoid an unaffordable computing time, we have used a propagation code developed in our previous work [19] that reduces the transport along the beam line to a problem of beam optics. In brief, a large number of particles is emitted for each scored particle, conserving the original energy, time and position at the scorer, but varying the direction isotropically within a cone aperture calculated according to the 0.6 degree acceptance of the first collimator. Then, a geometrical algorithm determines for each particle if it passes through all the collimators and ends up reaching the experimental area. The necessary input values are therefore the diameters and positions of the collimators. The only assumption in this method is that the particles are emitted isotropically with a small variation in angle. In fig. 5 one can appreciate how this condition is fulfilled for a cone aperture of 4 degrees in the full neutron energy range. The main drawback of the geometrical transport is the absence of information about the background induced by neutron and photon interactions with the collimators, since they are considered *ideal*; but this contribution is discussed already in detail by Barros *et al.* [11] and is not relevant for the results presented in this work.

2.3 Geant4 physics lists

Geant4 v10.1 provides a wide variety of physics models that apply in different energy regimes. Therefore, for each particular physics simulation problem the user must choose an appropriate combination of models covering the full range of particles and energies of interest. In our case, neutron production via spallation is described basically as

a two-stage process: intranuclear cascade and subsequent de-excitation.

In our previous work on n_TOF-EAR1 [19] the Geant4 simulations with different combinations of models were compared to experimental data [20]. These consisted of the officially released *Physics Lists* (PL) that combine the Fritiof model (FTFP) [21,22] or the Quark-Gluon-String model (QGSP) [23] for the inelastic scattering of protons above 9 GeV with three different cascade models covering the energy range from 20 MeV to 9 GeV: the Liège Intranuclear Cascade model INCL++ [24,25], the Bertini (BERT) [26] or the Binary Cascade model (BIC) [23]. The last two models include a preequilibrium stage after the intranuclear cascade; in all cases, equilibrium de-excitation takes place at the end, including models which describe particle and photon evaporation, Fermi Break-up, multifragmentation and fission. The simulation of the n_TOF neutron production has been performed with the native de-excitation model, *G4ExcitationHandler*, which provided better agreement with the experimental data in EAR1 than the old version of the *ABLA* model [27] included in Geant4. Below 20 MeV, neutron-induced reactions are in all cases simulated by means of the G4NeutronHP module, using the evaluated data libraries (ENDF/B-VII.0 [25] in our case) available via the IAEA website [28] . Last, we have also considered the Geant4 built-in special treatment of the Thermal Scattering of neutrons below 4 eV (hereafter named HPT) [18], that considers the molecular properties of several materials when treating the neutron scattering, H_2O being the most relevant for our simulations.

One of the main objectives of the Geant4 simulations is to compare the results from diffent PL with the experimental neutron flux, especially regarding the shape of the energy distribution. Since there is no experimental data published yet for EAR2, we have chosen as a reference FTFP INCL++ HPT, that provided the best agreement with the experimental data for n_TOF-EAR1 regarding both the energy dependence and absolute value of the neutron flux[1]. This choice is justified according to the results for the neutron flux at n_TOF-EAR2, presented in fig. 6, which show that the relative deviations between different PL follow the same trends observed in EAR1 [19]. On the other hand, the choice of PL does not play such a significant role with respect to the results concerning the γ-ray background, the resolution function or the beam profile.

3 Neutron flux

The neutron flux is here defined as the number of neutrons integrated over the full spatial beam profile arriving at the experimental hall with a given energy. Its magnitude and energy dependence determine the type of experiments that can be performed and the energy ranges that can be covered at a given neutron beam facility. In the case of n_TOF-EAR2, it was indeed the enhancement of the neutron flux with respect to EAR1, by reducing the flight path from 185 to 18.5 meters, the main reason for its construction.

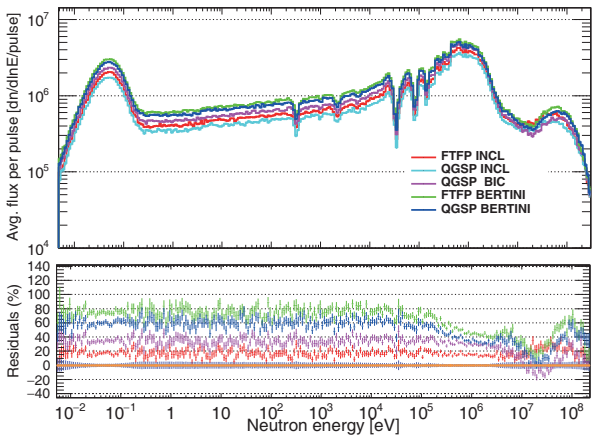

Fig. 6. Top: average neutron flux per pulse at n_TOF-EAR2 obtained with the different Geant4 Physics Lists (PL). Bottom: Ratio to QGSP INCL, the PL with the lowest integral flux.

Concerning the flux it is important to distinguish between average neutron flux per pulse, average neutron flux per second, and instantaneous neutron flux. The first two are related to each other by the frequency of the pulsed neutron beam, while the third takes into consideration not only the number of neutrons per pulse but also the time duration of the pulse itself and the flight path. In brief, the average neutron flux gives an indication on how long it takes to perform a given experiment at a facility and therefore on its feasibility, while the instantaneous flux determines the signal to background ratio in the case of radioactive samples.

In the following we discuss the average neutron flux per pulse and its neutron energy dependence, while later in this section we present both the average and instantaneous neutron flux compared to other time-of-flight facilities. The detailed values of average and instantaneous neutron flux are given in table 1.

3.1 Average neutron flux and energy dependence

The neutron flux per pulse, considering the nominal proton pulse intensity of $7 \cdot 10^{12}$ protons/pulse, is calculated from the output of the simulation registered at the EAR2 3D scorer after transport to the measuring station (see sects. 2.1 and 2.2). From now on, the neutron energies given in all figures correspond, as in our experiments, not to the neutron energy itself but to the neutron energy reconstructed from the corresponding time of flight; in this way directly comparable to experimental results.

The average neutron flux per pulse at n_TOF-EAR2 is displayed in fig. 6 for the different PLs, showing that

[1] In the meantime, we have found that the combination of QGSP and INCL++ provides an even better agreement with the experimental flux in EAR1 in terms of absolute value, giving the smallest absolute flux. The same situation is found in EAR2 as one can see in fig. 6.

Table 1. Summary of the beam characteristics as a function of the neutron energy.

	Neutron flux per pulse		γ-ray flux*	BIF @19.6 m	RF broadening ($\Delta E/E$)	
	$dn/d\ln E$	dn/dt (μs)	$d\gamma/d\ln E$/pulse	(20 mm diam.)	FWHM	FWTM
10 meV	$1.7 \cdot 10^5$	$1.1 \cdot 10^1$	0	0.45	$1.6 \cdot 10^{-2}$	$2.0 \cdot 10^{-1}$
100 meV	$6.4 \cdot 10^5$	$1.3 \cdot 10^2$	$1.6 \cdot 10^4$	0.46	$1.6 \cdot 10^{-2}$	$8.8 \cdot 10^{-2}$
1 eV	$2.4 \cdot 10^5$	$1.5 \cdot 10^2$	$1.1 \cdot 10^5$	0.45	$4.8 \cdot 10^{-3}$	$2.2 \cdot 10^{-2}$
10 eV	$2.2 \cdot 10^5$	$4.3 \cdot 10^2$	$2.0 \cdot 10^5$	0.45	$5.7 \cdot 10^{-3}$	$2.3 \cdot 10^{-2}$
100 eV	$2.2 \cdot 10^5$	$1.3 \cdot 10^3$	$1.9 \cdot 10^5$	0.45	$8.1 \cdot 10^{-2}$	$2.8 \cdot 10^{-2}$
1 keV	$3.0 \cdot 10^5$	$5.8 \cdot 10^3$	$1.4 \cdot 10^5$	0.45	$1.4 \cdot 10^{-2}$	$3.6 \cdot 10^{-2}$
10 keV	$4.8 \cdot 10^5$	$3.0 \cdot 10^4$	$7.4 \cdot 10^4$	0.44	$2.3 \cdot 10^{-2}$	$6.0 \cdot 10^{-2}$
100 keV	$5.8 \cdot 10^5$	$1.1 \cdot 10^5$	$3.6 \cdot 10^4$	0.48	$4.6 \cdot 10^{-2}$	$1.4 \cdot 10^{-1}$
1 MeV	$1.7 \cdot 10^6$	$1.2 \cdot 10^6$	$1.4 \cdot 10^4$	0.49	$5.6 \cdot 10^{-2}$	$1.2 \cdot 10^{-1}$
10 MeV	$2.2 \cdot 10^5$	$4.1 \cdot 10^5$	$8.6 \cdot 10^3$	0.47	$7.1 \cdot 10^{-2}$	$1.4 \cdot 10^{-1}$
100 MeV	$3.7 \cdot 10^5$	$2.3 \cdot 10^6$	$5.7 \cdot 10^4$	0.42	$1.8 \cdot 10^{-1}$	$3.5 \cdot 10^{-1}$

* Only photons with energies larger than 100 keV are considered.

deviations up to 80% in the absolute value of the neutron flux were found between the investigated high-energy hadronic models. Regarding the shape of the energy distribution, differences appear just above a few hundred keV, as in EAR1 [19]. The neutron energies in EAR2 span over eleven orders of magnitude between meV to a maximum energy of ~ 300 MeV. This high energy limit is lower than the ~ 10 GeV reached in EAR1 because the EAR2 beam line is perpendicular to the incident proton beam and thus it does not "see" the fast neutron component, forward emitted according to the kinematics of the spallation reactions.

The main features in the neutron energy distribution are the thermal peak in the tens of meV region, the isolethargic epithermal region between a few eV and tens of keV, which then overlaps with the evaporation peak in the MeV region and part of the spallation neutrons in the hundreds of MeV region. In addition, the aluminium layers around the spallation target and along the beam line are responsible for a series of transmission dips in the flux due to the ^{27}Al resonances at 35, 86, 146 keV and so on.

3.2 Instantaneous neutron flux: implications for radioactive samples

As stated before, not only the average neutron flux but also the instantaneous flux is an important parameter of a time-of-flight facility. In order to discuss these values we include in the following a comparison between the currently most competitive time-of-flight facilities worldwide featuring white neutron beams: n_TOF-EAR1 [6] at CERN (Switzerland), GELINA [8] at IRMM (Belgium), ANNRI [9] at J-PARC (Japan) and DANCE [10] at LANL (USA).

Figure 7 compares the average flux per pulse (top) and per second (middle), and the instantaneous flux (bottom), of these facilities, including for completeness the

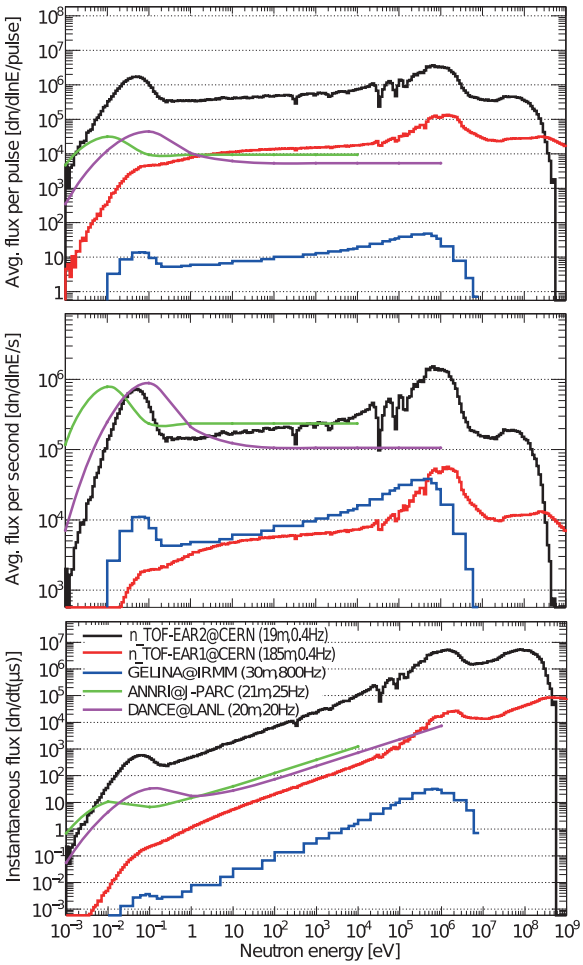

Fig. 7. The neutron flux at n_TOF-EAR2 compared to n_TOF-EAR1, GELINA, DANCE and ANNRI. The neutron flux is expressed in the form of average neutron flux per pulse (top), average neutron flux per second (middle) and instantaneous neutron flux per pulse (bottom).

flight path lengths and pulse frequencies in the legend. As expected, the spallation sources with short flight paths (n_TOF-EAR2, ANNRI and DANCE) reach the highest fluxes per pulse, gaining a factor 25–30 in flux per pulse with respect to n_TOF-EAR1. GELINA, the only non-spallation neutron source in the comparison, deserves some further comments. At its 30 m beam line, GELINA presents the lowest average neutron flux per pulse, but it makes it up with its high repetition rate and equals n_TOF-EAR1 when it comes to average flux per second. In addition to the mentioned beam line at 30 m, it has several measuring stations with flight paths between 10 and 400 m, reaching the highest flux at the 12.5 m station, which is about two times larger than the one shown in fig. 7.

It has been mentioned already that it is the instantaneous neutron flux what plays a major role in measurements on radioactive samples. For instance, in a recent time-of-flight measurement of ^{240}Pu(n, f) [29] at n_TOF-EAR1 with a sample of 3.2 mg and an activity of 27 MBq, the α and spontaneous fission decay channels induced a background much higher than the neutron-induced fission, preventing a succesful measurement. A new measurement already ongoing at n_TOF-EAR2 has demonstrated [30] that the gain of a factor $\sim$ 300 in instantaneous neutron flux with respect to EAR1 (see bottom panel in fig. 7) solves this issue, making the experiment well feasible. Indeed, the new 18.5 m long neutron beam line at n_TOF features the highest instantaneous white neutron flux worldwide, which makes it specially well suited for measuring highly radioactive samples, for which several measurement proposals have been already approved by the *CERN Isolde and NTOF Committee (CERN-INTC)*.

4 Spatial beam profile

The shape of the beam is dictated by the collimation system, and changes with the distance from the last collimator, as shown in fig. 8. The beam diverges from a 22 mm diameter flat beam at the exit of the collimator (18.05 m flight path) to a Gaussian-like neutron beam with a FWTM of 36 and 50 mm at flight paths of 19.5 and 20.5 m, respectively. The detailed values of the beam size (FWHM and FWTM) as a function of the vertical flight path are displayed in fig. 9.

Quite often, measurements are performed with samples that are smaller than the beam. In these cases, the samples will see only a fraction of the beam, known as the beam interception factor (F_{bif}) and usually determined experimentally through the Saturated Resonance Method [31]. Another option is to determine F_{bif} experimentally as the ratio of the reaction yields measured with the sample shape of interest and with a sample larger than the Both methods allow one to determine the F_{bif} at certain neutron energies, but the F_{bif} changes slightly with neutron energy, as neutrons of different energies may have different origins at the spallation target. We have thus calculated F_{bif} as a function of neutron energy for different sample diameters for a flight path of 19.6 m, the

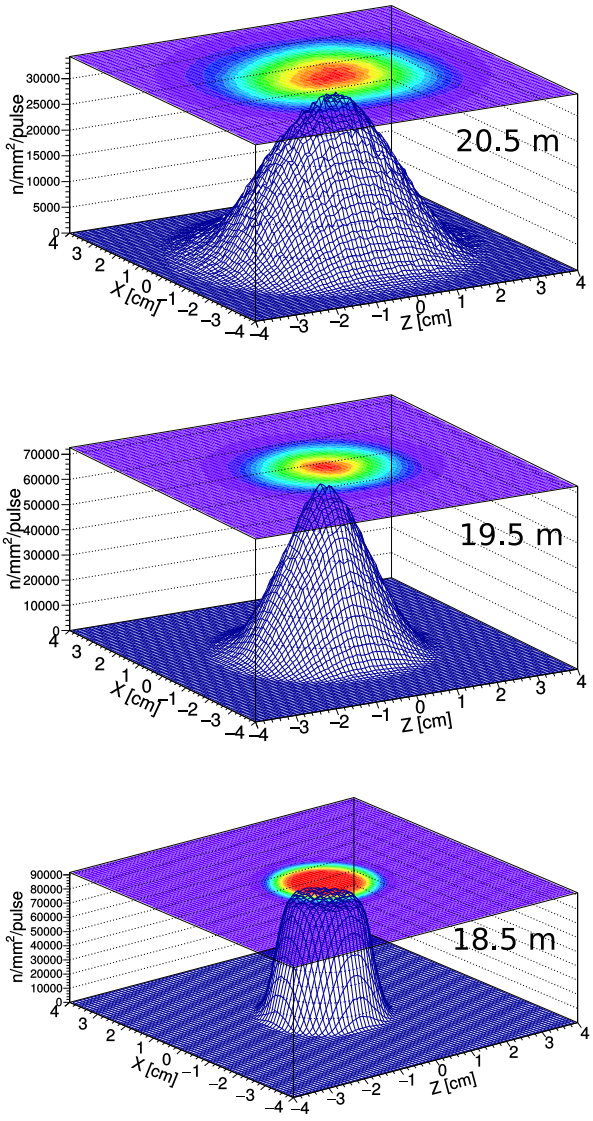

Fig. 8. Beam profile in EAR2 at different flight paths.

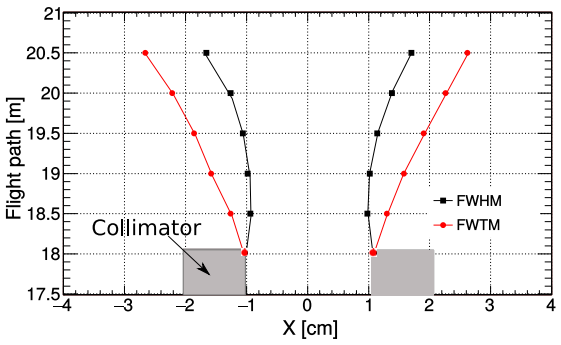

Fig. 9. Limits of the neutron beam profile at one half (FWHM) and one tenth (FWTM) of the maximum for different flight path distances along EAR2. Note that the last collimator ends at 18.05 m.

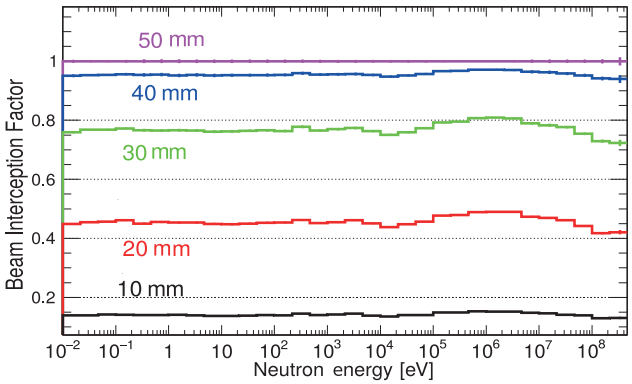

Fig. 10. Beam interception factor (F_{bif}) at the nominal position for neutron capture experiments (19.6 m) for different sample diameter values.

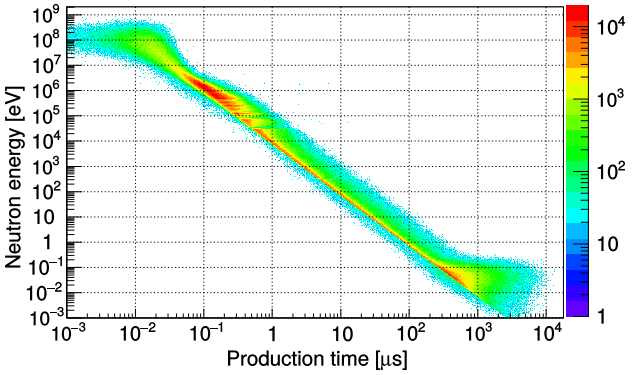

Fig. 11. Resolution function of the n_TOF-EAR2 neutron beam expressed in the form of neutron energy *vs. production time* (*i.e.* time of arrival to a plane 1.5 m above the center of the target).

reference position for neutron capture experiments. The results, displayed in fig. 10 and summarized in table 1, exhibit a fairly flat behavior in the full energy range, confirming that the directionality plays a less important role compared to EAR1 [19]. However, one can appreciate a maximum increase of up to 10% for a 20 mm diameter sample in the energy range correspondig to the evaporation peak. The lowest F_{bif} is obtained for the fastests neutrons. This result is related to the fact that fast neutrons are produced directly along the way of the proton beam axis, off-centered and orthogonal with respect to the vertical beam line of EAR2.

5 Resolution function and resonance broadening

A common feature of neutron time-of-flight facilities is the fact that all the neutrons of a given energy do not exit the target-moderator assembly at the same time, thus making the time-to-energy relation non-univocal. The relation between these two quantities is known as the Resolution Function (RF) of the facility and it can only be determined by means of simulations, which can then be validated with experimental data.

In the following we refer to *production time* as the time it takes, after the proton beam impinges the target, for a neutron to be generated, moderated and transported outside the spallation target assembly, until it is scored at the intersection of the beam line with an orthogonal plane 150 cm above the center of the spallation target. The spread of the production times for a given neutron energy is related to the spread of the original charged particle beam, the neutron production mechanism, and the neutron moderation. The latter two effects are related to the composition and size of the spallation target and the moderation system. This spread in the *production time* for a given neutron energy introduces a broadening in the structures or resonances observed in time-of-flight experiments.

In the case of n_TOF-EAR2, the Gaussian time distribution of the incident proton beam has a width $\sigma = 7$ ns, the size of the lead target is 40 cm in length with a diameter of 60 cm, and the thickness of both the water moderator layer and the Al vessel is 3 cm. The resulting RF is displayed in fig. 11, which contains only the neutrons arriving to EAR2. In this figure one can already see that the relative time spread is larger for thermal energies and above 10 MeV and consequently these energy ranges present a lower energy resolution, as it is summarized in table 1.

In order to illustrate and discuss the effect of the RF on the resonance shape, fig. 12 shows a set of resonances in the evaluated neutron capture cross sections of several isotopes (^{25}Mg, ^{56}Fe and ^{197}Au) between tens of eV and 100 keV. Each panel displays the Doppler broadened cross section of interest and the corresponding shape obtained with the RF resulting from our simulation, showing that the asymmetric broadening and the energy shift introduced by the RF. This broadening is such that, beyond a given energy (that depends on the level spacing of the isotope under study), resonances can no longer be distinguished from neighbouring ones, making it difficult to analyse individual resonances. Beyond this energy measured cross sections have to be analyzed with a formalism adequate for the Unresolved Resonance Region [32].

A summary of the resolution broadening as a function of neutron energy is given in table 1. The energy resolution is better than 1% in the eV-keV region (0.5% at 1 eV) and increases to 2% at 10 keV and nearly 6% at 1 MeV, showing the more limited capability for resolving individual resonances at high energies compared to n_TOF-EAR1 [19].

6 In beam γ-ray background

6.1 γ-ray flux

Photons are produced along with neutrons as spallation reaction products as well as in capture reactions occurring

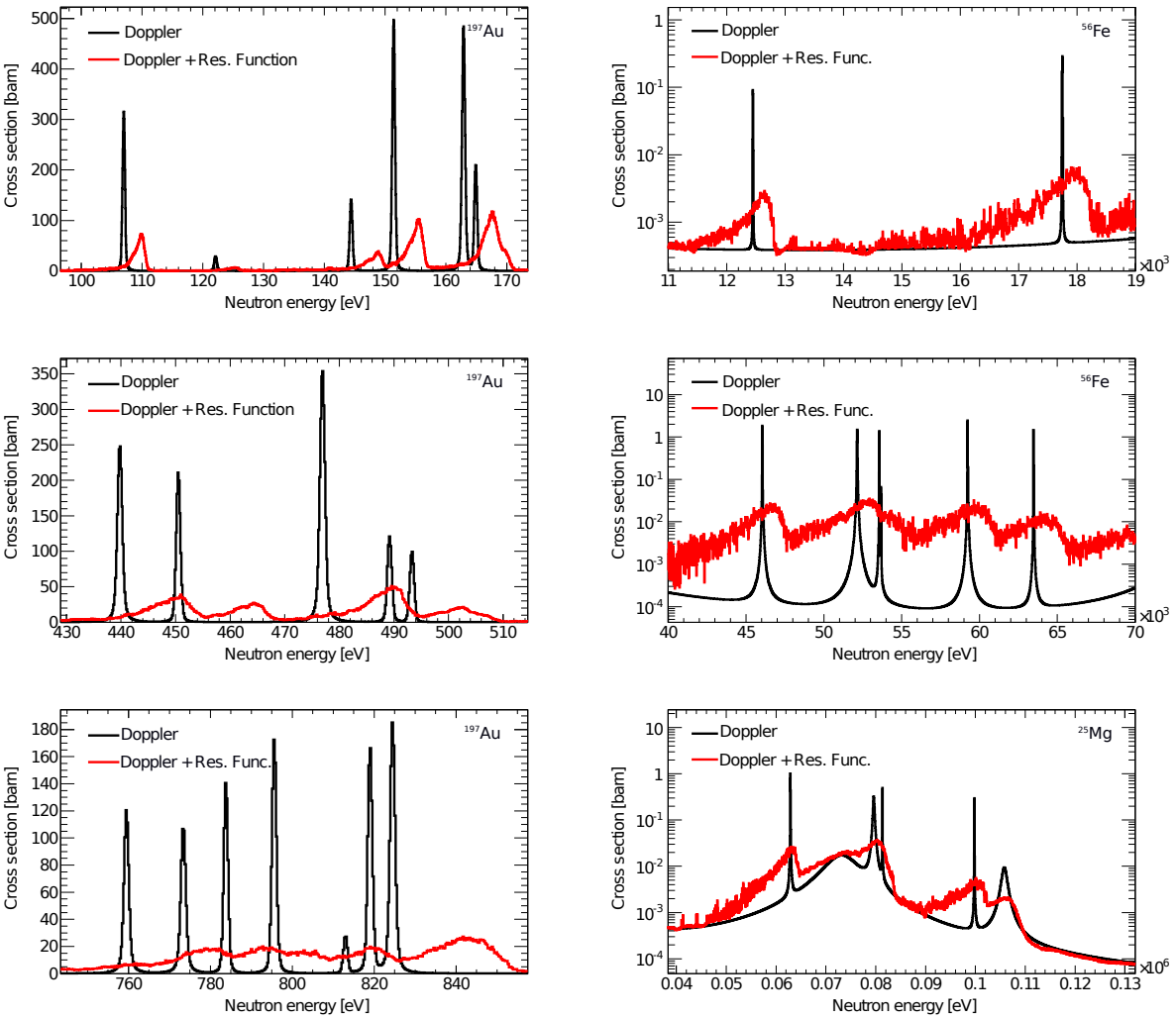

Fig. 12. Illustration of the resolution broadening for different resonances in the evaluated cross sections of ^{25}Mg, ^{56}Fe and ^{197}Au. The energy ranges are chosen to illustrate the energies at which the resonances start to overlap due to resolution broadening.

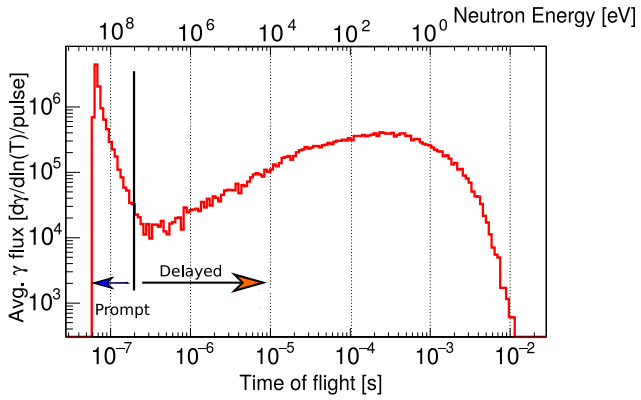

Fig. 13. Distribution of in-beam γ-rays as a function of time-of-flight, where both the prompt (< 200 ns) and delayed (> 200 ns) components can be distinguished. TOF-reconstructed neutron energies are indicated as a reference

within the target/moderator assembly. As shown in fig. 13, the first γ-ray component is emitted prompt with the arrival of the proton beam and arrives at EAR2 in less than ~ 200 ns, but no less than the 66 ns needed to travel the 19.6 m flight path at the speed of light. The γ-rays arriving after ~ 200 ns are produced during the moderation process, up to a maximum delay of 10 ms and peaking around 500 μs, which corresponds to a TOF-reconstructed neutron energy of ~ 10 eV.

The γ-ray energy distribution of these two components, shown in fig. 14, is quite different (although not as much as in EAR1, see refs. [6,19]). The prompt component has less peak structure than the delayed one and reaches energies up to 100 MeV. The delayed component shows well defined γ-rays belonging to cascades from (n,γ) reactions, mainly the 2.2 and 7.4 MeV lines from capture in hydrogen and aluminium. What is absent, as compared to EAR1, is the 478 keV line from ^{10}B(n,α) reactions because the moderator in EAR2 consists only of water, and not borated water like in EAR1.

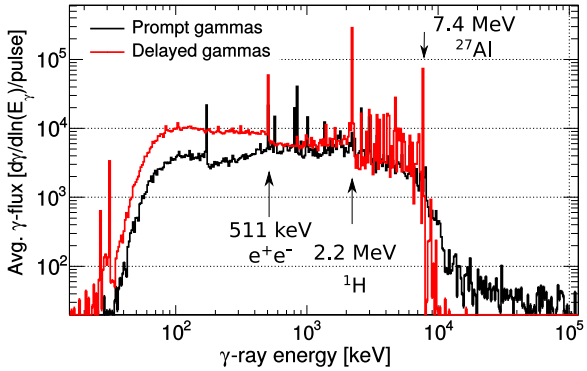

Fig. 14. Energy distribution of the prompt and delayed γ-ray components, including indications of the most prominent γ-rays from capture reactions and the annihilation peak.

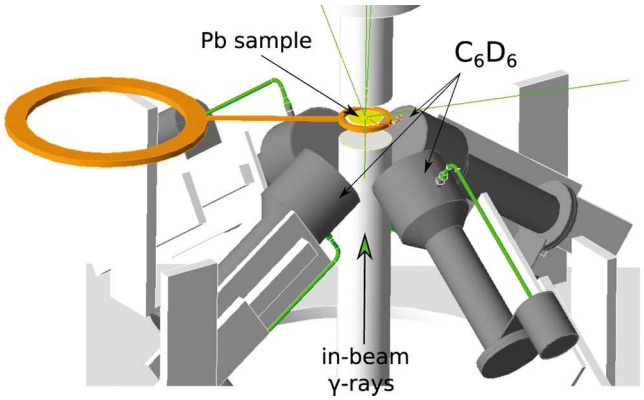

Fig. 15. The Geant4 model of the capture setup in EAR2 consisting of four C_6D_6 detectors placed at 10 cm from a Pb sample. The in-beam γ-rays are scattered in the Pb sample and the energy deposited by the backscattered photons is registered in the detectors.

6.2 γ-ray background in (n, γ) measurements

This γ-ray background is not relevant when measuring cross sections of reactions with charged particles in the exit channel, (n,f) or (n,p/α), but becomes very important for neutron capture measurements. Indeed, it can become the main source of background in an experiment (see, for instance, ref. [33]) because it is difficult to distinguish these photons from the capture γ-rays from the investigated sample. However, the γ-rays arriving at the detectors are Compton scattered in the sample, thus loosing part of their energy and therefore their original energy structure. In the active volume of the C_6D_6 detectors the scattered photons deposit part of their energy by a further Compton scattering. As a result, the energy distribution of the in-beam γ-rays, of the backscattered photons, and the deposited energy in the C_6D_6 detectors look very different. We have performed a full simulation of the process, the in-beam γ-rays being scattered on a 1 mm lead sample and then entering and being detected in a setup for capture measurements made of four of the new n_TOF C_6D_6 detectors with reduced neutron sensitivity [34]. The

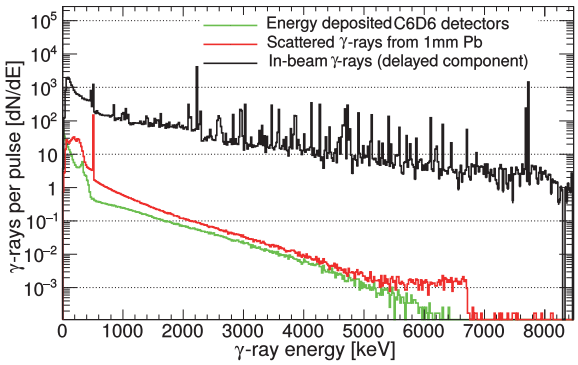

Fig. 16. Energy spectra of the delayed in-beam γ-rays compared to the energy distribution of the fraction arriving at the C_6D_6 detectors after scattering on a 1 mm thick Pb sample and the energy they finally deposit in these detectors.

simulated geometry is shown in fig. 15 and the results are displayed in fig. 16, demonstrating what has been discussed above about the lower energy and loss of energy structures. These results indicate that setting a minimum detection threshold just above 511 keV already eliminates 93% of the in-beam γ-ray–induced background.

7 Summary and conclusions

We have simulated with the Geant4 toolkit the neutron beam of the n_TOF-EAR2 facility at CERN. The goal of these simulations is to provide a tool for both the analysis of the commissioning experiments and the planning of the upcoming physics measurements. The characteristics studied are neutron flux and beam profile, the resolution function and in-beam γ-ray background.

The results and the comparison of the flux with other time-of-flight facilities confirm the outstanding instantaneous flux of more than 10^5 n/μs/pulse in the keV region reached at n_TOF-EAR2, while still keeping a reasonable energy resolution. It has been illustrated that the divergence of the beam along the flight path is sizable, and that the ten times shorter flight path entails a limitation for resolving individual resonances due to a loss of resolution compared to n_TOF-EAR1. The in-beam γ-ray component has been studied and its effect on neutron capture experiments has been discussed. A summary of the main properties of the facility concerning the neutron and γ-ray flux, the beam interception factor for a 20 mm diameter sample, and the resolution broadening is given in table 1.

Overall, Geant4 has proven to be a very powerful tool for the simulation of neutron production and transport, and thus the results of this work are already being used by the members of the n_TOF Collaboration for analysis and planning of experiments.

We acknowledge the n_TOF Collaboration. The research that led to these results has received funding from the EC FP7 Programme under the projects NEUTANDALUS (Grant No.

334315) and CHANDA (Grant No. 605203), and the Spanish Ministry of Economy and Competitiveness projects FPA2011-28770-C3-02, FPA2013-45083-P and FPA2014-53290-C2-2-P. The simulations have been performed at the computing cluster FIS-ATOM and we would like to acknowledge the staff of the Centro Informático y Científico de Andaluca (CICA) working on its mantainance.

References

1. WPEC Subgroup 31 (SG31), *Meeting Nuclear Data Needs for Advanced Reactor Systems* (Nuclear Energy Agency, OECD, 2014) NEA/NSC/WPEC/DOC(2014)446.
2. U. Fischer *et al.*, Nucl. Data Sheets **120**, 226 (2014).
3. F. Kaeppeler, R. Gallino, S. Bisterzo, W. Aoki, Rev. Mod. Phys. **83**, 157 (2011).
4. A.L. Nichols, R. Capote, Nucl. Data Sheets **120**, 239 (2014).
5. J.T. Goorley, W.S. Kiger III, R.G. Zamenhof, Med. Phys. **29**, 145 (2002).
6. The n_TOF Collaboration (C. Guerrero *et al.*), Eur. Phys. J. A **49**, 27 (2013).
7. C. Weiss *et al.*, Nucl. Instrum. Methods A **799**, 90 (2015).
8. D. Ene, C. Borcea, S. Kopecky, W. Mondelaers, A. Negret, A.J.M. Plompen, Nucl. Instrum. Methods A **618**, 54 (2010).
9. K. Kino *et al.*, Nucl. Instrum. Methods A **626**, 58 (2011).
10. P. Koehler, Nucl. Instrum. Methods A **292**, 541 (1990).
11. S. Barros, I. Bergstrom, V. Vlachoudis, C. Weiss *et al.*, JINST **10**, P09003 (2015).
12. `http://www.fluka.org`.
13. G. Battistoni *et al.*, AIP Conf. Proc. **896**, 31 (2007).
14. A. Ferrari *et al.*, *FLUKA: A Multi-Particle Transport Code*, CERN-2005-10, INFN/TC_05/11, SLAC-R-773 (2005).
15. H. Iwase, K. Niita, T. Nakamura, J. Nucl. Sci. Technol. **39**, 1142 (2002).
16. D.B. Pelowitz (Editor), *MCNPX User's Manual, Version 2.7.0*, Los Alamos National Laboratory report, LA-CP-11-00438 (2011).
17. S. Agostinelli *et al.*, Nucl. Instrum. Methods A **506**, 250 (2003).
18. E. Mendoza, D. Cano-Ott, T. Koi, C. Guerrero, IEEE Trans. Nucl. Sci. **61**, 2357 (2014).
19. S. Lo Meo, M.A. Cortés-Giraldo, C. Massimi, J. Lerendegui-Marco *et al.*, Eur. Phys. J. A **51**, 160 (2015).
20. The n_TOF Collaboration (M. Barbagallo *et al.*), Eur. Phys. J. A **49**, 156 (2013).
21. B. Andersson *et al.*, Nucl. Phys. B **281**, 289 (1987).
22. B. Nilsson *et al.*, Comput. Phys. Commun. **43**, 387 (1987).
23. GEANT4 Physics Reference and User Manuals, available at `http://geant4.cern.ch`.
24. A. Boudard *et al.*, Phys. Rev. C **87**, 014606 (2013).
25. D. Mancusi *et al.*, Phys. Rev. C **90**, 054602 (2014).
26. A. Heikkinen *et al.*, *Bertini intra-nuclear cascade implementation in Geant4*, in *Computing in High Energy and Nuclear Physics (CHEP 2003), La Jolla, California, March 24–28, 2003*, `http://arxiv.org/abs/nucl-th/0306008v1`.
27. A. Kelíc *et al.*, Report INDC(NDC) **0530**, 181 (2008).
28. `www-nds.iaea.org/geant4/`.
29. A. Tsinganis, E. Berthoumieux, M. Calviani, V. Vlachoudis, the n_TOF Collaboration, *Measurement of the $^{240,242}Pu(n,f)$ reaction cross-section at n_TOF*, CERN-INTC-2010-042.
30. A. Tsinganis *et al.*, *Measurement of the $^{240}Pu(n,f)$ cross-section at the CERN n_TOF facility: first results from Experimental Area II (EAR-2)*, in *Proceedings of the 14th International Conference on Nuclear Reaction Mechanisms, Varenna, Italy, June 15–19, 2015*, edited by F. Cerutti *et al.*, CERN-Proceedings-2005-001.
31. R. Macklin, J. Halperin, R. Winters, Nucl. Instrum. Methods A **164**, 213 (1979).
32. F.H. Frohner, *Evaluation and Analysis of Nuclear Resonance Data*, JEFF Report 18, NEA/OECD (2000).
33. G. Tagliente *et al.*, Phys Rev. C **77**, 035802 (2008).
34. P. Mastinu *et al.*, *New C_6D_6 detectors: reduced neutron sensitivity and improved safety*, CERN-n_TOF-PUB-2013-002 (2013).